Chemical routes to materials

Unveiling the potential of (CoFeNiMnCr)₃O₄ high-entropy oxide synthesized from CoFeNiMnCr high-entropy alloy for efficient oxygen-evolution reaction

Barbara Ljubec Božiček[1,2,*], Jitka Hreščak[7], Monika Kušter[1,2], Janez Kovač[3], Iztok Naglič[4], Boštjan Markoli[4], Barbara Šetina Batič[5], Martin Šala[6], Sandra Drev[7], Živa Marinko[1], Miran Čeh[1,7,*], and Belisa Alcantara Marinho[1,*]

[1] *Department for Nanostructured Materials, Jožef Stefan Institute, Jamova 39, 1000 Ljubljana, Slovenia*

[2] *Jožef Stefan International Postgraduate School, Jamova 39, 1000 Ljubljana, Slovenia*

[3] *Department of Surface Engineering, Jožef Stefan Institute, Jamova 39, 1000 Ljubljana, Slovenia*

[4] *Department of Materials and Metallurgy, Faculty of Natural Sciences and Engineering, University of Ljubljana, Aškerčeva Cesta 12, 1000 Ljubljana, Slovenia*

[5] *Vacuum Science and Optoelectronics, Institute of Metals and Technology, Lepi Pot 11, 1000 Ljubljana, Slovenia*

[6] *Department of Analytical Chemistry, National Institute of Chemistry, Hajdrihova 19, 1001 Ljubljana, Slovenia*

[7] *Center for Electron Microscopy and Microanalysis, Jožef Stefan Institute, Jamova 39, 1000 Ljubljana, Slovenia*

ABSTRACT

Electrochemical water-splitting is a promising green technology for the production of hydrogen. One of the bottlenecks, however, is the oxygen evolution half-reaction (OER), which could be overcome with the development of a suitable electrocatalyst. Recently, non-noble metal, high-entropy oxides (HEO) have been investigated as potential OER electrocatalysts, but complex synthesis approaches that usually produce the material in powder form limit their wider utilization. Here, an innovative synthesis strategy of formulating a nanostructured (CoFeNiMnCr)₃O₄ HEO thin film on a CoFeNiMnCr high entropy alloy (HEA) using facile electrochemical and thermal treatment methods is presented. The CoFeNiMnCr HEA serves as exceptional support to be electrochemically treated in an ethylene glycol electrolyte with ammonium fluoride to form a rough and microporous structure with nanopits. The electrochemically treated CoFeNiMnCr HEA surface is more prone to oxidation during a low-temperature thermal treatment, leading to the growth of a spinel (CoFeNiMnCr)₃O₄ HEO thin film. The (CoFeNiMnCr)₃O₄ HEO exhibits a superior overpotential of 341 mV at 10 mA cm⁻² and a Tafel slope of 50 mV dec⁻¹ along with remarkable long-term stability in alkaline media. The excellent catalytic activity and stability for the OER can serve as a promising platform for the practical utilization of (CoFeNiMnCr)₃O₄ HEO.

🍬 Springer

GRAPHICAL ABSTRACT
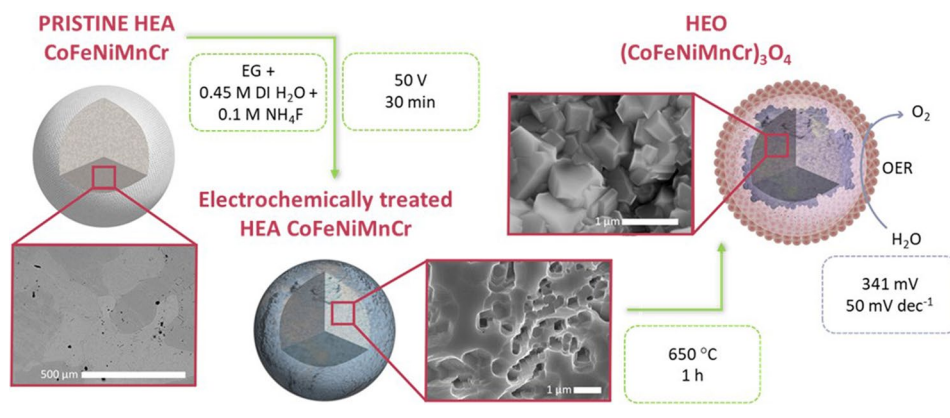
Introduction

Global energy consumption is rapidly expanding to satisfy the demands of an increasing human population [1]. The dominant source of energy is still fossil fuels (coal, oil, and natural gas), as a consequence of their availability and convenient management [2]. However, fossil fuels are associated with environmental pollution and climate change. Hence, the development and utilization of novel energy technologies from renewable sources are of great importance to achieve clean energy. Electrochemical water-splitting is considered a promising environmental approach to address this problem [3].

Water-splitting consists of two principal half-reactions, i.e., the hydrogen and oxygen evolution reactions (HER and OER) as two-electron and four-electron transfers occurring on the cathode and anode, respectively [4]. One of the bottlenecks with water-splitting is the OER due to the intrinsically sluggish reaction kinetics, requiring a high reaction potential to overcome the activation barrier for generating the molecular oxygen [5].

Until now, iridium-based materials were considered as the standard electrocatalysts for the OER, as they exhibit excellent catalytic activity and stability [6]. However, the high price and scarcity severely hinder their industrial application [7]. Therefore, substantial efforts are being put into developing effective, stable, available, and affordable electrocatalysts.

Transitional metals, including Co, Fe, Ni, Mn and their corresponding oxides, are promising electrocatalysts for the OER; however, their poor electrocatalytic properties continue to limit the complete replacement of noble-metal electrocatalysts [8, 9]. Recently, high-entropy materials (HEMs), including high-entropy alloys (HEAs) and high-entropy oxides (HEOs), were suggested as a new platform for screening efficient electrocatalysts, as the high-entropy effect enables the incorporation of five or more elements in (near)equimolar ratios, offering more opportunities to tune the catalytic properties than conventional single-metal-, bimetallic-, and trimetallic-based electrocatalysts [10–12].

Among the HEMs, HEAs are the most widely investigated electrocatalysts for the OER [13]. Bulk HEAs possess some appealing advantages of exceptional physical and electrochemical properties (e.g., a high hardness and compressive strength, good corrosion and oxidation resistance, and a high thermal and electrical conductivity), but the limited specific and electrochemically active surface area inhibits their OER enhancements. Therefore, two approaches are currently employed to overcome these limitations, i.e., utilization of electrodes composed of different supports (carbon, nickel foam, etc.) with applied nanoparticulate HEAs or usage of various surface treatment methods to obtain multiple metal oxides or hydroxides on bulk HEAs as electrode supports [14]. The first approach suffers from insufficient electrical conductivity due to the interfacial resistance between the support and the nanoparticulate HEA, as well as nanoparticulate HEAs can be easily separated from the support during the OER, resulting in environmental pollution [15]. While, the (hydro)

oxide layer on a surface-treated HEA support can be subject to microstructural and chemical changes during the OER, which leads to a lower stability and is thus unsuitable for industrial applications [16, 17]. Therefore, developing an integrated electrode with dense active sites and high activity and conductivity is highly desirable.

Recently, the suitability of HEOs as electrocatalysts was investigated in OER research. For example, Talluri et al. used a facile, soft-chemical process to synthesize a spinel $(CoCrFeMnNi)_3O_4$ HEO with a low overpotential of 220 mV at 10 mA cm^{-2}, a Tafel slope of 100 mV dec^{-1} and good stability over 9 h [18]. The same group also reported that a spinel $(CoCrFeMnNi)_3O_4$ HEO, produced using a reverse coprecipitation approach followed by a 750 °C heat treatment, exhibited a low charge transfer resistance of 1.56 Ω [19]. A study published by Wang et al. introduced a low-temperature approach to preparing a similar spinel (Co, Cu, Fe, Mn, Ni)$_3O_4$ HEO, which achieved 10 mA cm^{-2} at 1.58 V in 1 M KOH [20]. There are literature reports on the excellent performance of HEOs in OER processes arising from the diverse electronic interactions of different elements within the entropy-stabilized structures. The activity and stability of some HEOs were found to be even higher than those of HEAs [21]. However, the synthesis strategies to obtain HEO electrocatalysts can be very complex, requiring multiple steps and extreme conditions of high temperature and pressure [22, 23]. Therefore, it is necessary to simplify and refine the synthesis strategies.

In line with all the abovementioned, this study aimed to synthesize a spinel $(CoFeNiMnCr)_3O_4$ HEO thin film on a CoFeNiMnCr HEA support using simple and cost-effective electrochemical and subsequent thermal treatment methods, and then to evaluate the performance of the resulting $(CoFeNiMnCr)_3O_4$ HEO electrocatalyst for the alkaline OER, as well as to compare it with a pristine CoFeNiMnCr HEA electrocatalyst.

Materials and methods

Preparation of pristine CoFeNiMnCr HEA

Raw materials (> 99.0 wt %) of Co, Fe, Ni, Mn, and Cr were used to prepare bulk CoFeNiMnCr HEA ingots with dimensions of 15 × 15 × 15 mm³. The melting was carried out in an alumina tube furnace at 1550 °C for 1 h under an argon (Ar) atmosphere (99.999%) with a cooling rate of 5 °C min^{-1}. The resulting ingots were annealed at 1000 °C for 25 h in an Ar atmosphere and then cooled to 800 °C with a cooling rate of 5 °C min^{-1}. The tube furnace was then opened and the alloy was rapidly cooled in water. The CoFeNiMnCr HEA ingots were randomly cut with a diamond saw (Buehler IsoMet 1000) under the rotation speed of 300 rpm. The cutting CoFeNiMnCr HEA specimens were attached to a disc grinder (Gatan Disc Grinder Model 623) and firstly manually ground with SiC abrasive paper (P1000, P1200, P2400, and P4000) in wet conditions, and then polished with 3 μm diamond emulsion to plan-parallel specimens with dimensions of 4 × 4 × 0.25 mm³. The specimens were then ultrasonically cleaned in ethanol for 5 min, and subsequently rinsed with distilled water, followed by drying in a stream of air.

Preparation of $(CoFeNiMnCr)_3O_4$ HEO thin film

The $(CoFeNiMnCr)_3O_4$ HEO thin film on CoFeNiMnCr HEA was prepared in two steps. First, the surface of pristine CoFeNiMnCr HEA was electrochemically treated in a two-electrode electrochemical cell using a TOE 8871 direct-current (DC) power supply (TOELLNER Electronic Instrumente GmbH). The pristine CoFeNiMnCr HEA and platinum foil (99.95%, Goodfellow Cambridge Ltd.) were used as the working and counter electrodes, respectively. A detailed description of the experimental setup can be found in our previous work [24]. The electrochemical surface treatment was performed at 50 V for 15–30 min in 20 mL of ethylene glycol (EG) (99.5%, Carlo Erba Reagents) electrolyte containing 0.1–0.45 M ultrapure H_2O (0.055 μS cm^{-1}) and 0.1–0.5 M ammonium fluoride (NH_4F) (99.99%, Sigma-Aldrich) at ambient temperature (approx. 20 °C). The selection of parameters was based on studies reporting the successful electrochemical treatment of surfaces of unitary (e.g., Co [25], Fe [26], Ni [27]), binary (e.g., Co–Ni [28]), or ternary (e.g., Co–Fe–Ni [29], stainless steel [30, 31]) alloys. The electrochemically treated surface of CoFeNiMnCr HEA had a circular area of approximately 0.071 cm². After the surface treatment, the specimens were rinsed with ethanol and distilled water. The as-obtained CoFeNiMnCr HEA was then thermally treated in a muffle furnace (Nabertherm GmbH) under an atmosphere of air at 250, 450, 650, or 850 °C with a cooling rate of 5 °C min^{-1}.

Chemical and physical characterization

The microstructure and chemical composition of the materials were characterized by scanning electron microscopy (SEM) using a Verios G4 HP microscope (Thermo Fisher Scientific Inc.) equipped with an Ultim Max SDD 65 mm^2 detector for energy-dispersive X-ray spectroscopy (EDXS) (Oxford Instruments AztecLive). The electron accelerating voltage was 20 kV. Detailed investigations of the prepared $(CoFeNiMnCr)_3O_4$ HEO lamella in cross-section orientation were performed with scanning transmission electron microscopy (STEM) on Spectra 300 (Thermo Fisher Scientific Inc.) equipped with 4 × 30 mm^2 windowless Super-X SDD EDXS detector. STEM images were recorded with a bright-field (BF) detector at an accelerating voltage of 200 kV. Also, selected area electron diffraction (SAED) was investigated using a conventional transmission electron microscope (TEM) JEM-2100 (Jeol Ltd.). The texture of the pristine CoFeNiMnCr HEA was assessed by electron-backscatter diffraction (EBSD) using a Hikari Super EBSD Camera. The EBSD data were analyzed using EDAX Orientation Imaging Microscopy Software. The phase compositions of the materials were determined by X-ray diffraction (XRD) using a Malvern Panalytical Empyrean X-ray diffractometer (Almelo, Netherlands) with a Cu-target tube (λ Kα1 = 0.15406 nm and λ Kα2 = 0.154439 nm) in the Bragg–Brentano geometry in the scan range of $10° < 2\theta < 90°$. The XRD spinning regime was applied for the investigation of the bulk pristine CoFeNiMnCr HEA using a monochromated X-ray beam and a divergence slit of 0.04 rad with a step size of 0.026° and a counting time of 1 s per step. Whereas, the XRD analysis of thin films formed after electrochemical and thermal treatment had a configuration Chi-Phi-x–y-z stage; theta/theta geometry by using a divergence slit of 0.04 rad, a step size of 0.02° and a mask of 10 mm on the incident beam path and a parallel plate collimator 0.27 on the diffracted beam path. The XRD data were analyzed using HighScore Plus XRD Analysis Software PDF-4 + . The information on the phase composition of the $(CoFeNiMnCr)_3O_4$ HEO thin film was obtained with a NTEGRA confocal Raman spectrometer at an excitation wavelength of 488 nm, an incident power of approximately 3 mW, a grating of 600 grooves mm^{-1} and an objective of 100 × at a spot size of 1 μm in the range 100–900 cm^{-1}. The chemical composition and the oxidation state of the elements on the surface and subsurface of materials were determined using a PHI-TFA XPS spectrometer (Physical Electronics Inc.) with an Al monochromatic X-ray source working at a pass energy of 58 eV. The XPS surface-analysis depth and area were up to 5 nm and 0.4 mm in diameter, respectively. The XPS depth analysis was performed using Ar$^+$ ions with an energy of 3 keV scanned over an area of 3×3 mm^2 with an effective sputtering rate of 3.3 nm min^{-1}. The sputtering rate was measured on the reference material made of a SiO$_2$ thin film on Si support with a thickness of 100 nm, which was confirmed by TEM analysis. The sputtering rate for other materials may differ by ± 30% from the reference material. Furthermore, the approximated surface free energy was determined with the Neumann Equation of State (EQS) model [32, 33] from the contact angle of ultrapure H$_2$O (0.055 μS cm^{-1}) on the solid surface of the pristine CoFeNiMnCr HEA and $(CoFeNiMnCr)_3O_4$ HEO thin film. The contact angles were determined with an Attension Theta Lite Optical Tensiometer (Biolin Scientific) at ambient temperature (approx. 20 °C) and relative humidity of 40–50%. A water droplet of 10 μL was deposited on the sample surface. The average contact angle was calculated using Attension Theta software. A 3D inverted optical profilometer (OP) Ametek Zygo Zegage PRO HR (Zygo Corporation) was used to determine the actual surface area of the materials. Lastly, the possible presence of metal ions in the electrolyte after the electrochemical surface treatment of the CoFeNiMnCr HEA was detected with inductively coupled plasma optical emission spectrometry (ICP-OES) using a Varian 715-ES spectrometer (Agilent Technologies, Inc) in semiquantitative mode.

Electrochemical characterization

All the electrochemical experiments were performed in 20 mL of 1 M KOH (≥ 85.0%, Merck) at ambient temperature (approx. 20 °C) and a starting pH of 13.5 in a three-electrode Teflon cell using a Palm-Sens4 potentiostat/galvanostat/impedance analyzer (PalmSense BV). A pristine CoFeNiMnCr HEA or $(CoFeNiMnCr)_3O_4$ HEO, a platinum mesh (Zlatarna Celje d.o.o.), and a reversible hydrogen electrode (RHE) Hydroflex (Gaskatel GmbH) were used as the working, counter, and reference electrodes, respectively. Samples were pre-activated for 500 cycles using cyclic voltammetry (CV) at a scan rate of 300 mV s^{-1} to obtain stable measurements. The onset potential and overpotential of the electrocatalysts

were estimated with linear-sweep voltammograms (LSVs). The LSV for the OER was conducted in the potential range 1.2–1.7 V at a scan rate of 20 mV s^{-1}. The electrochemical double-layer capacitance (C_{dl}) can be evaluated with different techniques that are in good agreement [34]. In this study, the CV experiments were performed at various scan rates, i.e., 2, 5, 10, 15, and 20 mV s^{-1} in the 1.12–1.17 V non-Faradaic potential window. The non-Faradaic potential was tracked with an open-circuit potential technique for 60 s. Next, C_{dl} was assessed from the slope of the linear regression between the working and counter current half differences in the middle of the potential window of the CV curves versus the scan rates. The obtained C_{dl} values were used to estimate the corresponding electrochemical active surface areas (EASAs) according to the equation EASA = C_{dl}/C_s, where a common specific capacitance C_s of 40 µF cm^{-2} was used [18]. The electrochemical impedance spectroscopy (EIS) was measured at a potential of 1.6 V over a frequency ranging from 0.1 to 10,000 Hz with an alternating-current (AC) amplitude of 10 mV. The measured EIS data were fitted with PSTrace software. The rigorous performance of the OER stability test is still under discussion [35]. Here, a chrono-amperometry test was performed at a potential of 1.6 V for 10 h. LSV and CV data were normalized to the actual surface areas of the working electrodes, which were determined with the previously mentioned optical profilometry. The ohmic potential resistance (iR) between the reference and working electrodes was measured with EIS at the open circuit potential. The iR compensation of 85% was applied during the electrochemical experiments in the positive feedback mode. The uncompensated iR value was about a few Ω. The indicated iR-compensation and LSV/CV-normalization approaches are decisive in properly determining the kinetic parameters of the electrochemical OER [36, 37].

Results and discussion

Characterization of pristine CoFeNiMnCr HEA

The microstructure of the pristine CoFeNiMnCr HEA consisted of up to a few 100 µm grains with a primary matrix phase and small amounts of secondary particles (Fig. 1a). The elemental composition of the CoFeNiMnCr matrix phase (Fig. S1a) measured by

EDXS point analysis was 20.4 ± 0.6 at % of Co, 20.3 ± 0.1 at % of Fe, 20.0 ± 0.1 at % of Ni, 19.0 ± 0.2 at % of Mn, and 20.3 ± 0.5 at % of Cr. The EDXS analysis thus confirmed that the composition of the matrix phase between and within different grains corresponded to the HEA equi-atomic solid solution of all five elements. Particles in the shapes of blocks and rods were observed within the grains and at the grain boundaries (inset of Fig. 1a). The EDXS mapping analysis showed that the indicated particles (Fig. S1a) were rich in Cr and depleted in Co, Fe, and Ni, while Mn was homogeneously distributed throughout the material. Additionally, the particles contained higher C and/or O levels relative to the matrix phase. The EBDS analysis of the matrix phase (Fig. S1b) confirmed the characteristic diffraction pattern of the face-centered cubic (FCC) unit cell. The diffraction patterns of some particles (Fig. S1b) corresponded to $M_{23}C_6$-type carbides, also with a FCC unit cell. The metal ion (M) present in the $M_{23}C_6$ carbide was mainly Cr, with less Mn, because of the higher chemical affinity of Cr for C leading to a more rapid chemical reaction between these two components, compared to Mn and C [38]. Nevertheless, the presence of Mn in the $M_{23}C_6$ carbide should not be neglected, due to the possible replacement of Cr by Mn when reaching the critical amount of C in the solid solution matrix. Moreover, ab-initio calculations of the incorporation of metallic elements in the carbides for AlCrFeMnMo HEA indicated that the carbide in this concentrated multi-metallic environment should be more realistically viewed as $(Cr,Mn)_{23}C_6$ or even $(Cr,Al,Mn,Mo)_{23}C_6$ [39]. Also, on the pristine CoFeNiMnCr HEA surface were noticed some MnS inclusions (Fig. S1c) as a consequence of raw-material contamination.

From the XRD diffractogram (Fig. S2) of the pristine CoFeNiMnCr HEA it is possible to observe a series of FCC diffraction peaks of the matrix phase at 43.54° (111), 50.75° (200), 74.69° (220) and 90.47° (311) with a lattice constant of 3.59 Å, along with some small $M_{23}C_6$-type carbide peaks (at 48.37°, 55.25°, 56.75°, 57.21°, 65.50°, and 77.67°), and Mn_2O_3 peaks (at 29.27°, 47.38°, 60.48°, and 64.28°) with a lattice constant of 10.65 Å and 9.41 Å, respectively. The higher peak intensity of the FCC solid solution matrix over the carbide and oxide particles indicated the dominance of the FCC solid solution, because physico-chemical criteria for the formation of isomorphous alloy are fulfilled [40].
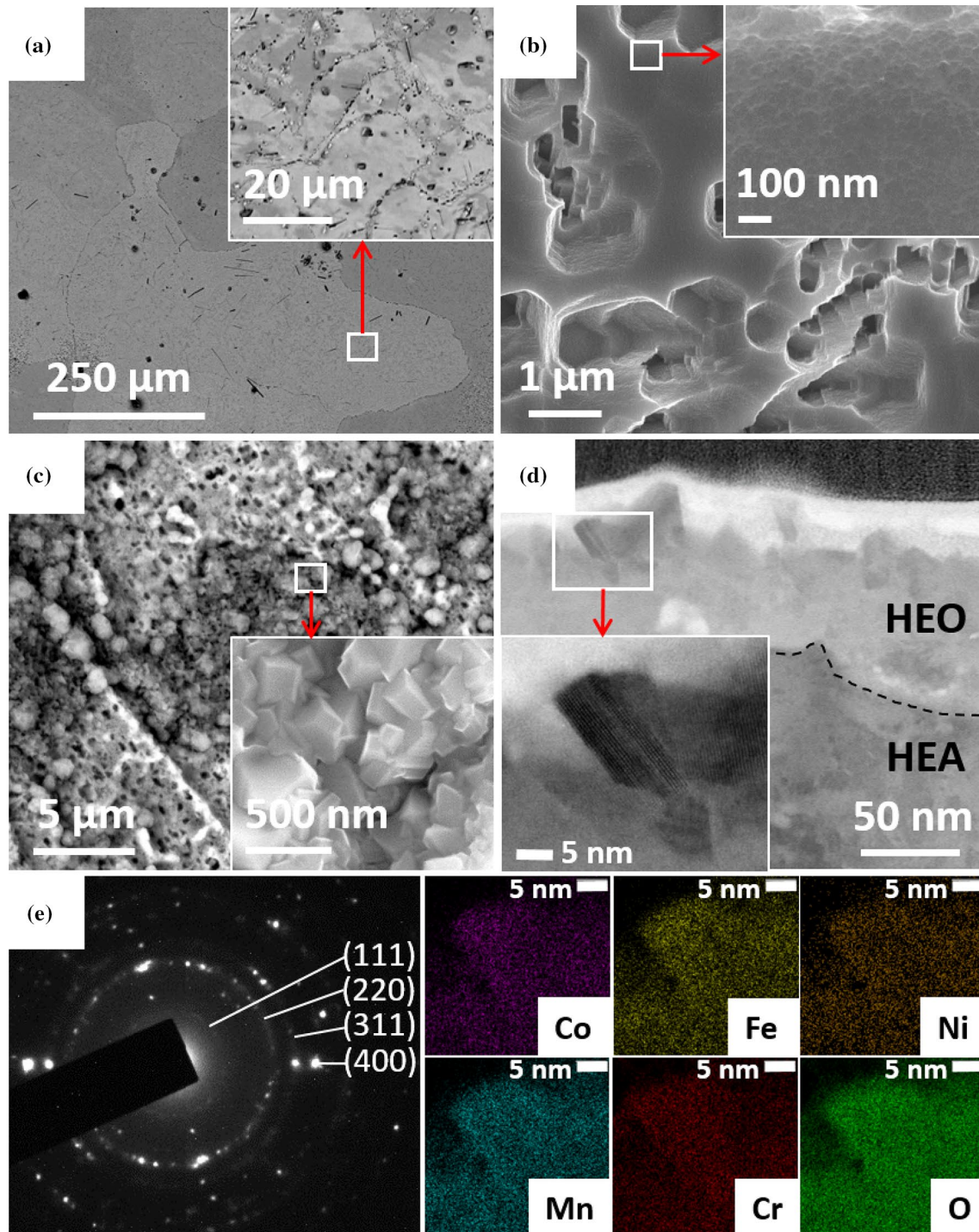
Figure 1 Top-view SEM image of **a** pristine CoFeNiMnCr HEA, **b** electrochemically treated CoFeNiMnCr HEA, and **c** $(CoFeNiMnCr)_3O_4$ HEO. **d** The cross-section BF-STEM image with EDXS elemental mapping, and **e** SAED pattern of $(CoFeNiMnCr)_3O_4$ HEO thin film.

A detailed description of XPS spectral deconvolution and interpretation can be found in the Supplementary material. As shown by the XPS survey (Fig. S3a) and high-resolution (Fig. S3b) spectra, the pristine CoFeNiMnCr HEA surface was composed of C, O and all five metallic elements. The O was mostly

in the form of surface oxygen (OH⁻) and less lattice oxygen (O^{2-}). Metallic elements Co ($Co^0/Co^{2+}/Co^{3+}$), Fe ($Fe^0/Fe^{2+}/Fe^{3+}$), Mn ($Mn^0/Mn^{2+}/Mn^{3+}/Mn^{4+}$) and Cr ($Cr^0/Cr^{3+}$) showed mixed valence states, while Ni was present only in the metallic state because it exhibits the lowest diffusivity and the highest activation energy of diffusion among other elements in CoFeNiMnCr HEA [41]. The presence of high-valenced metallic elements was also a consequence of the natural passivation of the material in air. Furthermore, the XPS depth profile (Fig. S3c) showed an enrichment with Cr, Mn, C, and O in the subsurface layer, which additionally confirmed the presence of the metallic carbide and oxide particles observed with other analyzing techniques. Carbide and oxide particles were often reported in CoFeNiMnCr HEAs due to contamination of the raw materials and contamination during the synthesis [42].

Formation and characterization of (CoFeNiMnCr)$_3$O$_4$ HEO

The (CoFeNiMnCr)$_3$O$_4$ HEO thin film on CoFeNiMnCr HEA was prepared with electrochemical and subsequent thermal treatment methods. SEM, STEM, XRD, XPS, Raman, OP, and ICP-OES analyses were performed to fully characterize the (CoFeNiMnCr)$_3$O$_4$ HEO thin film.

Electrochemical treatment

The experiments for the electrochemical treatment of the CoFeNiMnCr HEA surface under different conditions mostly yielded no changes in the CoFeNiMnCr HEA surface microstructure or led to a severe dissolution of the metal ions in the electrolyte, coloring the electrolyte yellowish and greenish, along with their deposition on the platinum counter electrode, forming a grayish layer on the surface of the platinum. However, pursuing the electrochemical treatment in EG electrolyte containing 0.45 M ultrapure H_2O and 0.1 M NH_4F at 50 V for 30 min at room temperature (approx. 20 °C) showed significant changes on the surface but still suppressed the severe dissolution of the metal ions in the electrolyte, as observed in other attempts.

The overall SEM image of the electrochemically treated CoFeNiMnCr HEA (Fig. 1b) showed randomly ordered micropores in various shapes and sizes. The distribution and dimensions of the micropores in electrochemically treated CoFeNiMnCr HEA were similar to the carbide and oxide particles in the pristine CoFeNiMnCr HEA, confirming their dissolution from the solid solution matrix into the electrolyte during the electrochemical treatment. It has been reported that Cr-carbides along the grain boundaries in austenitic stainless steel experience easy anodic dissolution because the aggressive electrolyte species create a separation or gap between the Cr carbide and the metal matrix due to the depletion of Cr [43]. Furthermore, detailed SEM images (inset of Fig. 1b) revealed a complete coverage of the electrochemically treated surface with nanopits, which were a consequence of pitting corrosion. It has been reported that 304-type stainless steel can suffer from pitting corrosion in halide-containing electrolytes under specific conditions, enhanced by the presence of impurities (e.g., MnS) on the surface [31], which have been also observed in pristine CoFeNiMnCr HEA.

The XRD pattern of the newly formed layer on the surface of the electrochemically treated CoFeNiMnCr HEA (Fig. S4) exhibited three FCC solid solution peaks with planes of atoms at 43.54° (111), the most noticeable 50.75° (200), and 74.69° (220) with the same lattice constant as pristine CoFeNiMnCr HEA. Other new small peaks at 34.87°, 35.95°, 40.51°, and 58.68° could be assigned to individual or mixed metal fluorides and constitute evidence of fluoride incorporation into the matrix. There were no peaks assigned to $M_{23}C_6$-type carbide and Mn_2O_3 as observed in pristine CoFeNiMnCr HEA, confirming their dissolution in the electrolyte during the electrochemical treatment.

The XPS survey (Fig. S5a) and high-resolution spectra (Fig. S5b) shown an altered surface composition after the electrochemical treatment. For detailed spectral comparison, see Supplementary material. In general, on the surface were present C, O, and all five metallic elements, already detected in the pristine CoFeNiMnCr HEA, and also electrolyte-derived F. Elements O and F were present in the form of mainly surface OH⁻ and lattice F⁻, respectively. Metallic elements Co ($Co^0/Co^{2+}/Co^{3+}$), Fe ($Fe^0/Fe^{2+}/Fe^{3+}$) and Mn ($Mn^0/Mn^{2+}/Mn^{3+}/Mn^{4+}$) stayed in the same mixed valence states, while Ni ($Ni^0/Ni^{2+}/Ni^{3+}$) partially and Cr (Cr^{6+}) completely oxidized during the electrochemical treatment. As shown by the thorough XPS and XRD analysis, the newly formed surface layer consisted of a mixture of metal fluorides, metal (hydro)oxides and metals [44]. Additionally, the XPS depth profile (Fig. S5c) revealed that the thickness of the newly formed surface layer was around 5 nm. This layer was

formed at the expense of the incorporation of mainly F^- ions from the electrolyte during the electrochemical treatment because F^- ions have strong penetration kinetics for oxide films [30]. Furthermore, the surface layer was enriched with Cr, because it shows a slow dissolution rate in halogen-containing electrolytes when compared to other elements [45].

The ICP-OES experiments revealed a small presence of metallic ions in the electrolyte after electrochemical treatment in nearly equimolar concentrations (Co: 33.0 ± 0.9 µmol, Fe: 37.1 ± 1.3 µmol, Ni: 32.4 ± 0.8 µmol, Mn: 30.1 ± 0.9 µmol, and Cr: 32.2 ± 1.0 µmol). Namely, when a voltage was applied to the electrochemical system, the F^- ions with a small radius migrated faster than the oxide ions and reached the metal surface first, causing the dissolution of carbide and oxide particles and continuing the pitting and thus dissolution of the five metal solid solution matrix. The latter could also be the reason for the severe unevenness of the surface after the electrochemical treatment due to the non-uniformly adsorbed F^- ions on the metal surface [46]. The electrochemical process probably stimulated a symmetric dissolution of all five elements to preserve their original atomic ratio [47]. The dissolution process proceeded until the surface layer enriched with chromium species was formed, which prevented the further inward diffusion of F^- ions and outward diffusion of metal cations [48].

Thermal treatment

After the electrochemical treatment, all the specimens were subjected to a thermal treatment at different temperatures. At 250 °C and 450 °C no changes in the surface microstructure were observed, while at 850 °C the EDXS mapping of the cross-section region (Fig. S6a) showed a sandwich structure with a few layers, each rich in a specific element. For example, the topmost layer was enriched with Mn oxide. This occurs because Mn ions exhibit the highest diffusivity, the lowest activation energy of diffusion, and the highest electronegativity difference to oxygen among elements in CoFeNiMnCr HEA, which results in a prioritized reaction with oxygen ions to form oxides [49]. Only the thermal treatment at 650 °C yielded the formation of a multi-element oxides thin film, for which we confirmed the presence of $(CoFeNiMnCr)_3O_4$ HEO. Also, the thermal treatment of the pristine CoFeNiMnCr HEA without a prior electrochemical surface

treatment was performed at 650 °C. In this case, only partial oxidation of the surface occurred and the EDXS mapping analysis (Fig. S6b) of the oxidized areas showed an enrichment with Mn. Therefore, a rigorous electrochemical pre-treatment of the surface was important for the complete oxidation of the surface and the formation of $(CoFeNiMnCr)_3O_4$ HEO during the thermal treatment.

The overall top-view SEM image of $(CoFeNiMnCr)_3O_4$ HEO (Fig. 1c) revealed complete coverage with discontinuous ball- and ribbon-type oxide morphologies. The observed surface structure (inset of Fig. 1c) consisted of nanocrystals of different sizes up to 500 nm. Also, the BF-STEM imaging of $(CoFeNiMnCr)_3O_4$ HEO thin film (Fig. 1d) showed a nanocrystalline structure. The EDXS surface point analysis of nanocrystals showed a composition of 6.95 ± 0.91 at % of Co, 7.85 ± 0.53 at % of Fe, 6.58 ± 0.92 at % of Ni, 11.35 ± 0.75 at % of Mn, 9.23 ± 1.05 at % of Cr and 51.90 ± 1.25 at % of O, as well as the EDXS elemental mapping of selected nanocrystals (inset of Fig. 1d) confirmed a homogeneous distribution of all five metallic elements. Furthermore, the SAED pattern of $(CoFeNiMnCr)_3O_4$ HEO thin film (Fig. 1e) consisted of rings with recognizable spots representative of nanocrystalline $(CoFeNiMnCr)_3O_4$ HEO. These results were in good agreement with those obtained by Tallury et al. [18] and Grzesik et al. [50], who prepared a single-phase spinel $(CoCrFeMnNi)_3O_4$ HEO in powder form with a soft-chemical process or in pellet form by solid-state synthesis, respectively. However, on the surface (Fig. S7) there were also some larger, compared to the rest of the microstructure, ball- and ribbon-type oxides in the few-micrometers range. The EDXS elemental mapping showed that the indicated ball-type oxides consisted mainly of Mn oxide, while the ribbon-type oxides were mainly Cr oxides. A plausible reason for the existence of the oxide features could be their growth from the remaining Mn and Cr carbide or oxide particles, which were insufficiently or unsuccessfully dissolved from the solid solution matrix of the pristine CoFeNiMnCr HEA surface into the electrolyte during the electrochemical treatment. Furthermore, the surface topography was changing in each step of treatment and is in detail shown in Supplementary material (Fig. S8a–c). The surface of $(CoFeNiMnCr)_3O_4$ HEO was around threefold larger than of pristine CoFeNiMnCr HEA.

The XRD pattern of the thin film (Fig. 2a) exhibited a series of cubic spinel oxide ($Fd\text{-}3\,m$) peaks (JCPDS

no. #96–591-0037) at 18.23° (111), 30.02 (220), 35.14° (311), 36.95° (222), 43.58° (400), 53.05° (422) and 74.92° (533) with a lattice constant of 8.44 Å. The XRD and SAED patterns were consistent. Some additional peaks at 32.35°, 47.23°, 48.55° and 56.81° corresponding to Mn_2O_3 (lattice constant of 9.41 Å) were also indicated. XRD studies confirmed the formation of a spinel $(CoFeNiMnCr)_3O_4$ HEO with some other secondary oxide phases. Additionally, some spinel oxide peaks were broadened due to the imperfect crystal lattice of the prepared $(CoFeNiMnCr)_3O_4$ HEO, indicating the presence of nanocrystals, which was confirmed by the SEM and STEM analysis. The peak broadening could also originate from characteristic chemical heterogeneity or lattice distortion in the $(CoFeNiMnCr)_3O_4$ HEO [51]. The presented XRD pattern of $(CoFeNiMnCr)_3O_4$ HEO was consistent with the same HEO prepared by other research groups with different synthesis methods [19, 23, 50].

The Raman spectrum (Fig. 2b) revealed eight main bands at 178, 318, 365, 482, 517, 635, 665, and 688 cm^{-1}. These results matched well with those reported for different analogous spinels (chromites, ferrites, and other spinels) [52]. The bands at 178, 318, 482, 517, 665, and 688 cm^{-1} could be attributed to the $1F_{2g}$, E_g, E_g, $2F_{2g}$, A_{1g}, and A_{1g} vibrational modes of the normal spinel structure, whereas the bands at 365 and 635 cm^{-1} could refer to the E_g and A_{1g} of an inverse spinel structure. However, slight shifts in the position of some bands could be ascribed to an optical phonon confinement in the case of nanocrystals [18].

The XPS depth profile (Fig. 2c) indicated a thickness of the $(CoFeNiMnCr)_3O_4$ HEO thin film around 100 nm and was consistent with STEM studies. The XPS survey (Fig. 2d) and high-resolution spectra (Fig. 2e) indicated the presence of C, O, and all five metallic elements, while the F signal was negligible, confirming its almost complete removal from the $(CoFeNiMnCr)_3O_4$ HEO thin film. The elements Na, Ca, and K were also detected due to surface contamination during the thermal treatment in the muffle furnace. The O 1s spectrum changed significantly after thermal treatment. There were three peaks at 529.3 eV, 531.8 eV, and 533.2 eV, corresponding to O^{2-}, OH^-, and physically adsorbed H_2O, respectively [53], where the highest peak was assigned to O^{2-} and then the OH^- state. The Co 2p spectrum showed doublet splitting peaks at 780.0 eV (satellite peak at 785.1 eV) and 798.6 eV (satellite peak at 803.2 eV) for Co^{2+}, and doublet splitting peaks at 781.5 eV (satellite peak at 786.9 eV) and 796.5 eV (satellite peak at 805.2 eV) for

Co^{3+} [25]. The Fe 2p spectrum was deconvoluted into doublet splitting peaks at 709.6 eV (satellite peak at 713.5 eV) and 723.6 V (satellite peak at 726.9 eV) for Fe^{2+}, and doublet splitting peaks at 711.1 eV (satellite peak at 714.6 eV) and 725.3 eV (satellite peak at 728.6 eV) for Fe^{3+} [54]. The Ni 2p spectrum showed low signal peaks, which could be deconvoluted into peaks at 855.0 eV for Ni^{2+} and 856.3 eV for Ni^{3+} [55]. The Mn 2p spectrum showed low-intensity doublet splitting peaks at 640.8 eV (satellite peak at 646.8 eV) and 652.4 eV for Mn^{2+}, doublet splitting peaks at 642.0 eV and 653.4 eV for Mn^{3+}, and doublet splitting peaks at 643.0 eV and 654.7 eV for Mn^{4+} [56]. Lastly, the Cr 2p spectrum showed doublet splitting peaks at 576.5 eV and 586.4 eV for Cr^{3+}, and doublet splitting peaks at 578.8 eV and 588.5 eV for Cr^{6+} [31]. The presence of a Cr^{6+} state was also reported for wet chemical-derived spinel spherical mesoporous $(Ni_{0.15}Co_{0.29}Cr_{0.13}Fe_{0.11}Mn_{0.32})_3O_4$ and mesoporous thin film $(Cr_{0.2}Mn_{0.2}Fe_{0.2}Co_{0.2}Ni_{0.2})_3O_4$ HEO [55, 56]. The XPS study of the $(CoCrFeMnNi)_3O_4$ HEO thin film clearly indicated the incorporation of metal cations in mixed valence states, i.e., in the + 2, + 3, or + 4 oxidation states, except for Cr^{3+}/Cr^{6+}, which was supposed to be the characteristic binding configuration in spinel oxides [57]. In general, it would be expected that the oxide anions (O^{2-}) occupy the FCC lattice points, while the bivalent cations (Co^{2+}, Fe^{2+}, Ni^{2+}, Mn^{2+}) occupy 1/8 of the tetrahedral voids, while tri- (Co^{3+}, Fe^{3+}, Ni^{3+}, Mn^{3+}, Cr^{3+}) or even tetravalent (Mn^{4+}) cations occupy 1/2 of the octahedral voids [58].

All the studies combined confirmed the formation of a $(CoFeNiMnCr)_3O_4$ HEO thin film along with some other secondary oxides on the CoFeNiMnCr HEA support with electrochemical and subsequent thermal treatment methods.

Electrochemical activity of CoFeNiMnCr HEA and $(CoCrFeMnNi)_3O_4$ HEO

The OER performances of the pristine CoFeNiMnCr HEA and $(CoCrFeMnNi)_3O_4$ HEO electrocatalysts on the CoFeNiMnCr HEA support were investigated and compared. The LSV curve (Fig. 3a) showed that the CoFeNiMnCr HEA required an onset potential of 1.591 V and an overpotential of 361 mV at a current density of 10 mA cm^{-2}, while the $(CoCrFeMnNi)_3O_4$ HEO showed a negative shift of the onset potential at 1.571 V, and a current density of 10 mA cm^{-2} was achieved at an overpotential of 341 mV. The OER kinetics of the CoFeNiMnCr HEA
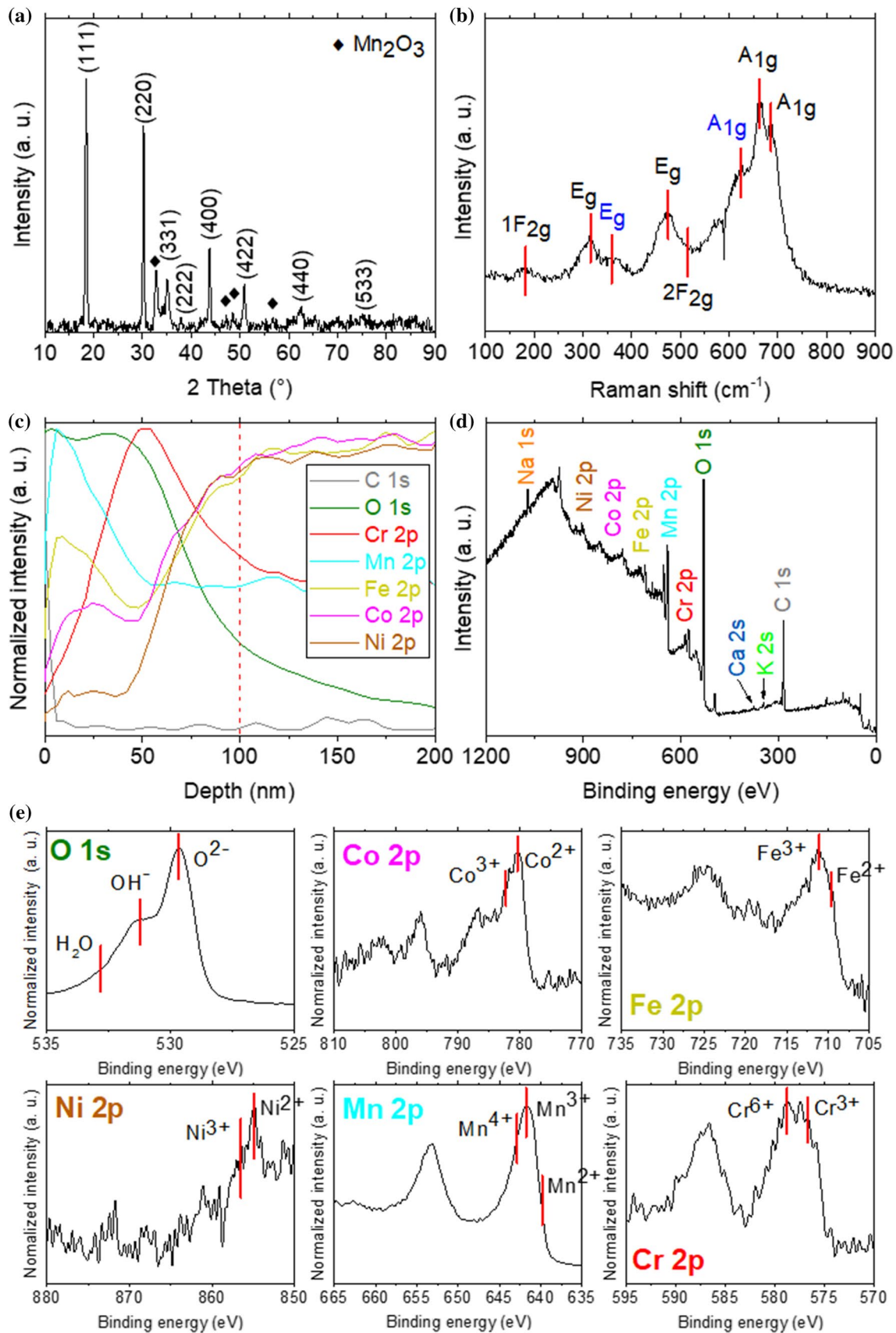
◄**Figure 2 a** XRD, **b** Raman pattern and XPS **c** depth profile, **d** survey spectrum, and **e** high-resolution spectra of (CoFeNiMnCr)$_3$O$_4$ HEO.

and (CoCrFeMnNi)$_3$O$_4$ HEO were analyzed in terms of Tafel plots (Fig. 3b) acquired from LSV curves. The Tafel slope was 65 mV dec^{-1} for the CoFeNiMnCr HEA and 50 mV dec^{-1} for the (CoCrFeMnNi)$_3$O$_4$ HEO. The Tafel slope could be correlated with the OER mechanism, but a few OER mechanisms are having various possible elementary steps, with any of them being the rate-determining step that changes as the pH of the electrolyte changes. Though it is hard to conclude about the mechanism based solely on the value of the Tafel slope [59]. Nevertheless, both the CoFeNiMnCr HEA and (CoCrFeMnNi)$_3$O$_4$ HEO exhibited a small Tafel slope, the (CoCrFeMnNi)$_3$O$_4$ with a smaller Tafel slope indicated a more rapid electron transfer at the electrode–electrolyte interface at the applied potentials, suggesting a better catalytic activity of the electrocatalyst [60]. EIS experiments were employed to additionally evaluate the electron-transfer kinetics before and after the surface treatment. Nyquist plots (Fig. 3c) for both the CoFeNiMnCr HEA and (CoCrFeMnNi)$_3$O$_4$ HEO could be elucidated with a Randle equivalent circuit, which consists of the electrolyte resistance (R_s), the charge-transfer resistance (R_{ct}) over the electrolyte–electrode interface and the double-layer, constant-phase element (CPE) [61]. The corresponding R_s for both the CoFeNiMnCr HEA and (CoCrFeMnNi)$_3$O$_4$ HEO was 35.5 Ω, which is considerably higher than in other reports [62, 63], probably due to a larger distance between the working and reference electrodes. The (CoCrFeMnNi)$_3$O$_4$ HEO exhibited a much lower R_{ct} of 18 Ω than the CoFeNiMnCr HEA (38 Ω), which should be attributed to the improved electron-transfer kinetics between the active sites on the (CoCrFeMnNi)$_3$O$_4$ HEO and the water intermediates [64].

To further explain the origin of the enhanced OER performance, it is necessary to appraise the exposed active sites from the EASA, which is related to the C_{dl} (Fig. 3d). The C_{dl} values for the CoFeNiMnCr HEA and (CoFeNiMnCr)$_3$O$_4$ HEO were 4.31 μF and 99.22 μF, respectively. The calculated EASA for the (CoFeNiMnCr)$_3$O$_4$ HEO was 2.48 cm^2, which is one order of magnitude higher than that of the CoFeNiMnCr HEA (0.11 cm^2). Here, the reported EASA values of the electrodes are a rough estimation. A proper

assessment of the EASA is still under discussion due to the challenge of identifying C_s. Therefore, it became common practice to use the average C_s value of 40 μF cm^{-2} for any material, independent of its nature and the experimental conditions, leading to an over or underestimation of the EASA values. To resolve this issue, it could be better to report the catalytic activity in terms of C_{dl} [65, 66]. However, since the measured C_{dl} value and the calculated EASA value were considerably higher for the (CoFeNiMnCr)$_3$O$_4$ HEO than the CoFeNiMnCr HEA, it can be concluded that the (CoFeNiMnCr)$_3$O$_4$ HEO contained more catalytically active sites to boost the OER activity.

The catalytic activity with respect to the OER could be additionally evaluated with the contact angle of the water [67]. It is commonly accepted that a material with a hydrophilic surface (contact angle < 90°) rather than a hydrophobic surface (contact angle > 90°) exhibits better reactivity with water. As shown, the contact angle is different. The contact angle for pristine CoFeNiMnCr HEA (Fig. S9a) was 95.3 ± 1.0°, indicating a slightly hydrophobic surface, and for the (CoFeNiMnCr)$_3$O$_4$ HEO (Fig. S9b) it was 73.2 ± 1.3°, indicating that the surface became hydrophilic. The hydrophilic nature of the (CoFeNiMnCr)$_3$O$_4$ HEO surface could be considered another reason for the improved catalytic properties [68]. Moreover, the decrease in the contact angle corresponded to the change in the chemical composition [69] of the surface after the treatment from the CoFeNiMnCr HEA to (CoFeNiMnCr)$_3$O$_4$ HEO. In addition to the contact angle, the surface free energy of the materials was calculated. The approximated surface free energies of the pristine CoFeNiMnCr HEA and (CoFeNiMnCr)$_3$O$_4$ HEO were 25.9 ± 0.6 mJ m^{-2} and 39.7 ± 0.8 mJ m^{-2}, respectively. The higher surface free energy of the (CoFeNiMnCr)$_3$O$_4$ HEO appeared to favor the OER.

Overall, the CoFeNiMnCr HEA and (CoFeNiMnCr)$_3$O$_4$ HEO exhibited an excellent OER performance, comparable or superior to analogous or similar HEA and HEO materials, and even to commercial RuO$_2$ powder (Table. S1). However, the (CoFeNiMnCr)$_3$O$_4$ HEO had better OER performance than the CoFeNiMnCr HEA due to an enlarged surface area with diverse nano- and microstructure, more complex chemical and electronic structures, and thus increased catalytically active sites. Referring to the first reason, both the physical and electrochemical surface areas of the (CoFeNiMnCr)$_3$O$_4$ HEO were one order of magnitude larger than that of the CoFeNiMnCr
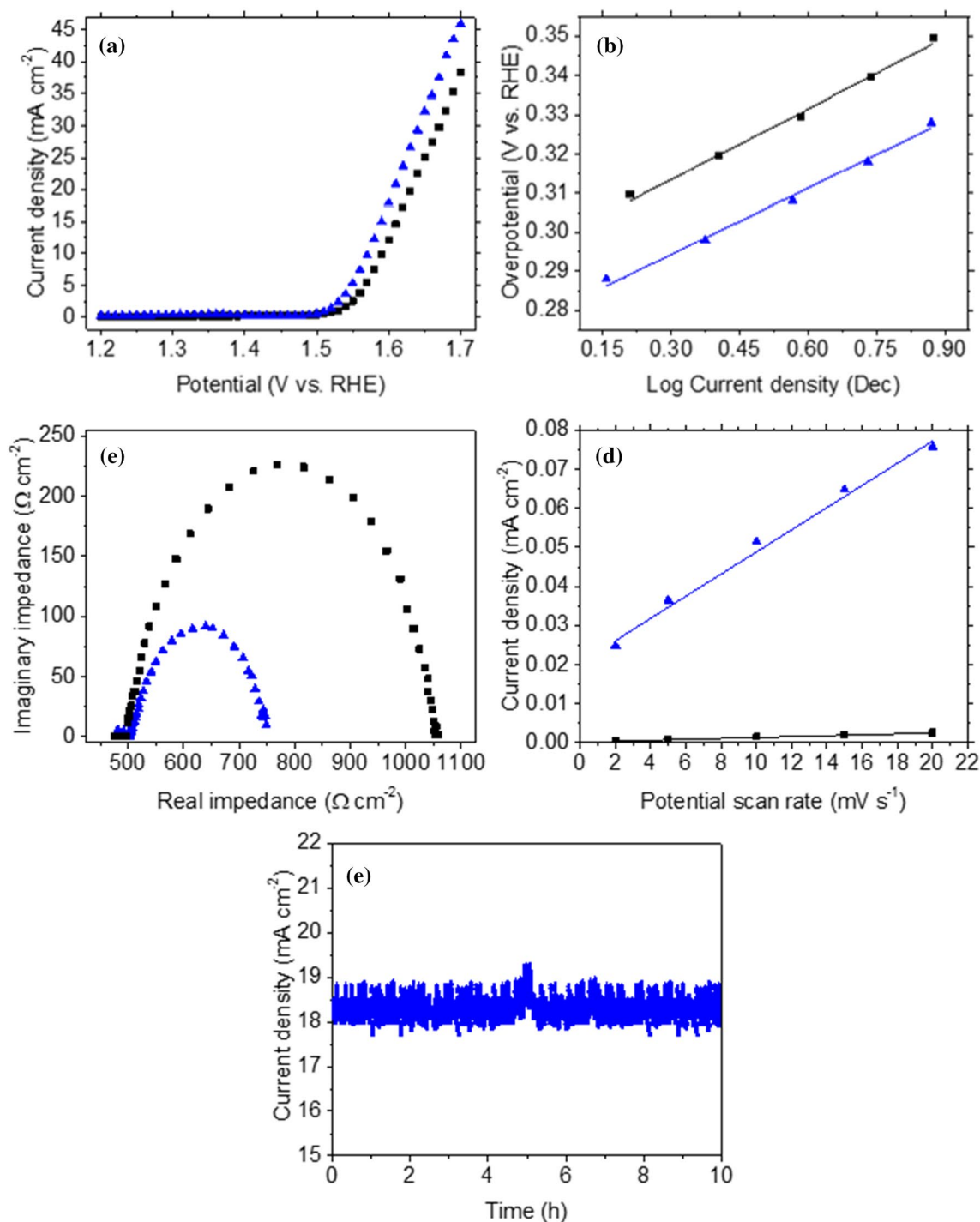
Figure 3 **a** LSV curves, **b** Tafel plots, **c** C_{dl}, **d** Nyquist plots, and **e** chrono-amperometry for (■) CoFeNiMnCr HEA, and (▲) (CoFeNiMnCr)$_3$O$_4$ HEO.

HEA. Since, it is well known that OER is a heterogeneous catalytic process taking place on the catalyst surface, increasing the catalyst's surface area leads to an increased number of catalytically active sites

available for reaction [70]. Regarding the second reason, both HEAs and HEOs exhibit severe lattice distortion induced by the atomic-size mismatch of the elements present, which could create significant residual

strains leading to a massive increase in the number of catalytically active sites [71]. However, the HEOs were additionally characterized by a charge-distortion effect, meaning an uneven electron-cloud distribution between the metal ions in different valence states and oxygen ions, which is anticipated to positively impact the catalytic reactions [72]. Lastly, as widely reported in the literature, the main active sites of catalysts (with activity decreasing in the following order) were oxygen vacancies, metal (hydro)oxides, and active metals. Metal (hydro)oxides not only participate in catalytic reactions but also produce abundant oxygen vacancies [67, 73]. In contrast, mono-metallic carbides showed negligible OER activities [74]. Since, the $(CoFeNiMnCr)_3O_4$ HEO consisted of oxygen vacancies and metal (hydro)oxides, while the CoFeNiMnCr HEA consisted of oxygen vacancies, metal (hydro)oxides, active metals, and metal carbides, it was somehow expected that the presence of more active sites with higher activity in the $(CoFeNiMnCr)_3O_4$ HEO than in the CoFeNiMnCr HEA would lead to enhanced OER performance.

Electrochemical stability of $(CoCrFeMnNi)_3O_4$ HEO

Structural and operating stability is another crucial parameter to evaluate the suitability of the material for OER applications. The long-term stability test (Fig. 3e) was performed solely on the $(CoFeNiMnCr)_3O_4$ HEO, since it showed a better electrocatalytic activity with respect to the OER than the CoFeNiMnCr HEA. In particular, the current density of approx. 18–19 mA cm^{-2} was maintained for 10 h. Only a small hump in the current density could be observed after 5 h. After the stability test, the electrochemical and physical characterization was repeated to fully evaluate the stability of the $(CoFeNiMnCr)_3O_4$ HEO. The onset potential and overpotential slightly (Fig. S8a) increased to 1.598 V and 368 mV at a current density of 10 mA cm^{-2}, respectively. The overpotential difference before and after the stability test was only 27 mV, indicating very good stability of the $(CoFeNiMnCr)_3O_4$ HEO, since the electrocatalyst is considered appropriate if the overpotential does not increase by more than 30 mV for over 10 h of chrono-amperometric experiments [59]. The Tafel slope (Fig. S8b) increased slightly from 50 to 55 mV dec^{-1} after the stability test. The C_{dl}

(Fig. S8c) and EASA decreased slightly to 55.2 µF and 1.38 cm^2, while R_{ct} (Fig. S8d) increased slightly to 25 Ω; however, still significantly better than the pristine CoFeNiMnCr HEA. The SEM image (Fig. S9b) showed no changes in the principal microstructure of the $(CoFeNiMnCr)_3O_4$ HEO after the stability test. Some new, quasi-spherical particles formed on top of the surface. According to the EDXS elemental mapping (Fig. S9), they belonged to the aforementioned oxidized impurities. The XRD pattern (Fig. S10b) changed slightly, meaning that only spinel oxide peaks at 18.23° (111), 35.14° (311), 36.95° (222), 43.58° (400), and 74.92° (533) were obtained, which is not unusual for such a complex structure. The XPS survey (Fig. S11a) and the high-resolution (Fig. S11b) spectra before and after the stability test were comparable. The XPS analysis confirmed the presence of O, Co, Fe, Ni, Mn, and Cr. Some previously discussed impurities were also detected. The only minor change was observed in the O, Co, and Cr 2p spectra. Particularly, in the O 1s spectrum, the intensity of the OH$^-$ peak decreased slightly, which could be attributed to the dissolution of the OH$^-$ species into the electrolyte. The Co 2p spectrum showed that the characteristic peaks for Co^{2+} increased slightly. The Cr 2p spectrum contained only low characteristic peaks for Cr^{3+}, because the Cr^{6+} ions dissolved into the strong alkaline electrolyte forming $[Cr(OH)_4]^-$ ions [17, 75]. Minor changes in electrochemical properties after the stability test could be connected to the presence of oxidized impurities (K, Na, Ca) on top of the $(CoFeNiMnCr)_3O_4$ HEO, which were incorporated into the oxide layer during the thermal treatment and then oxidized during the electrochemical experiments, blocking the highly active catalytic sites of $(CoFeNiMnCr)_3O_4$ HEO, while themselves being less electrocatalytically active with respect to the OER. An additional oxide layer formed at the expense of the oxidized impurities, which are poor conductors or insulators, hinders the charge transfer across the electrolyte–electrode interface [76]. Furthermore, the dissolution of Cr^{6+}, along with OH$^-$ ions could also contribute to slight changes after the stability test [77]. However, the aforementioned results indicate the very good stability of the $(CoFeNiMnCr)_3O_4$ HEO under a high voltage, which is believed to be induced by the characteristic core effects of HEO materials, i.e., high-entropy, sluggish diffusion, and the cocktail effect [73].

Conclusions

This study showed a state-of-the-art and facile synthesis approach for the development of a spinel $(CoFeNiMnCr)_3O_4$ HEO thin film on an immediately available, conductive CoFeNiMnCr HEA support with excellent activity and stability with respect to the OER process. The following conclusions could be drawn:

(1) The pristine CoFeNiMnCr HEA, as an electrode support, was successfully produced in an alumina tube furnace, yielding a fully crystallized material with a primary equi-atomic solid solution matrix and secondary carbide/oxide particles.

(2) A novel two-step synthesis approach was successfully employed to grow a $(CoFeNiMnCr)_3O_4$ HEO thin film on a CoFeNiMnCr HEA support. The first step included the electrochemical surface treatment, where the native surface contamination layer was removed as well as carbide and oxide particles were dissolved from the solid solution matrix of the CoFeNiMnCr HEA support, creating a suitable rough surface with micropores and nanopits. In the second step, an electrochemically treated CoFeNiMnCr HEA support was subjected to a thermal treatment in air at a low temperature of 650 °C resulting in the formation of the $(CoFeNiMnCr)_3O_4$ HEO.

(3) Different microscopic and spectroscopic analyses (SEM with EDXS, XRD, Raman, XPS) confirmed the presence of a nanothick film (around 100 nm) of cubic spinel $(CoFeNiMnCr)_3O_4$ HEO in the form of nanocrystals along with secondary oxide phases on the CoFeNiMnCr HEA support.

(4) The use of the $(CoFeNiMnCr)_3O_4$ HEO electrode for OER in 1 M KOH revealed a very small overpotential (341 mV at 10 mA cm^{-2}) and Tafel slope (50 mV dec^{-1}), increased C_{dl} (99.22 μF) and EASA (2.48 cm^2), and thus a decreased electrode resistivity (18 Ω). The surface of the $(CoFeNiMnCr)_3O_4$ HEO exhibited hydrophilic behavior (contact angle of 73.2°) with a surface free energy of 39.7 mJ m^{-2}.

(5) The $(CoFeNiMnCr)_3O_4$ HEO displayed better performance with respect to OER than the CoFeNiMnCr HEA due to more favorable structural and (electro)chemical characteristics. In particular, $(CoFeNiMnCr)_3O_4$ HEO had a larger exposed physical and electrochemically active surface area, a hydrophilic surface and thus a higher surface free energy. This was combined with a complex spinel HEO structure, having severe lattice and charge distortion and thus rich in oxygen vacancies, metal (hydro)oxides and active metals. All these features in combination, created multiple, highly active, catalytic sites for enhanced OER activity.

(6) The characteristic high-entropy, sluggish diffusion, and the cocktail effect contributed to excellent (electro)chemical and structural stability for the $(CoFeNiMnCr)_3O_4$ HEO with respect to long-term OER experiments.

Author contributions

BL Božiček involved in conceptualization, data curation, formal analysis, methodology, writing—original draft. J Hreščak involved in formal analysis, methodology. M Kušter involved in formal analysis, methodology. J Kovač involved in formal analysis, methodology. I Naglič involved in formal analysis, investigation, methodology, validation. B Markoli involved in resources, visualization, writing—review and editing. BŠ Batič involved in formal analysis, methodology. M Šala involved in formal analysis, methodology. S Drev involved in formal analysis, methodology. Ž Marinko involved in data curation, visualization. M Čeh involved in funding acquisition, methodology, project administration, resources, supervision, visualization, writing—review and editing. BA Marinho involved in conceptualization, funding acquisition, methodology, project administration, supervision, writing—review and editing.

Data availability

Data will be made available to readers upon request.

Declarations

Conflict of interest There are no conflicts of interests.

Ethical approval Not applicable.

Supplementary Information The online version contains supplementary material available at https://doi.org/10.1007/s10853-024-09710-5.

References

[1] Asif M, Muneer T (2007) Energy supply, its demand and security issues for developed and emerging economies. Renew Sustain Energy Rev 11:1388–1413. https://doi.org/10.1016/J.RSER.2005.12.004

[2] Pareek A, Dom R, Gupta J, Chandran J, Adepu V, Borse PH (2020) Insights into renewable hydrogen energy: recent advances and prospects. Mater Sci Energy Technol 3:319–327. https://doi.org/10.1016/J.MSET.2019.12.002

[3] Tarhan C, Çil MA (2021) A study on hydrogen, the clean energy of the future: hydrogen storage methods. J Energy Storage 40:102676. https://doi.org/10.1016/J.EST.2021.102676

[4] Ďurovič M, Hnát J, Bouzek K (2021) Electrocatalysts for the hydrogen evolution reaction in alkaline and neutral media. A comparative review. J Power Sources 493:229708. https://doi.org/10.1016/J.JPOWSOUR.2021.229708

[5] Xie X, Du L, Yan L, Park S, Qiu Y, Sokolowski J, Wang W, Shao Y, Xie X, Yan L, Park S, Qiu Y, Sokolowski J, Wang W, Shao Y, Du L (2022) Oxygen evolution reaction in alkaline environment: material challenges and solutions. Adv Funct Mater 32:2110036. https://doi.org/10.1002/ADFM.202110036

[6] Cherevko S, Geiger S, Kasian O, Kulyk N, Grote JP, Savan A, Shrestha BR, Merzlikin S, Breitbach B, Ludwig A, Mayrhofer KJJ (2016) Oxygen and hydrogen evolution reactions on Ru, RuO2, Ir, and IrO2 thin film electrodes in acidic and alkaline electrolytes: a comparative study on activity and stability. Catal Today 262:170–180. https://doi.org/10.1016/J.CATTOD.2015.08.014

[7] Qu HY, He X, Wang Y, Hou S (2021) Electrocatalysis for the oxygen evolution reaction in acidic media: progress and challenges. Appl Sci 11:4320. https://doi.org/10.3390/APP11104320

[8] Zhang K, Zou R, Zhang K, Zou R (2021) Advanced transition metal-based OER electrocatalysts: current status, opportunities, and challenges. Small 17:2100129. https://doi.org/10.1002/SMLL.202100129

[9] Rani A, Reddy R, Sharma U, Mukherjee P, Mishra P, Kuila A, Sim LC, Saravanan P (2018) A review on the progress of nanostructure materials for energy harnessing and environmental remediation. J Nanostructure Chem 8:255–291. https://doi.org/10.1007/S40097-018-0278-1

[10] Xin Y, Li S, Qian Y, Zhu W, Yuan H, Jiang P, Guo R, Wang L (2020) High-entropy alloys as a platform for catalysis: progress, challenges, and opportunities. ACS Catal 10:11280–11306. https://doi.org/10.1021/ACSCATAL.0C03617

[11] Chen YY, Duval T, Hung UD, Yeh JW, Shih HC (2005) Microstructure and electrochemical properties of high entropy alloys—a comparison with type-304 stainless steel. Corros Sci 47:2257–2279. https://doi.org/10.1016/J.CORSCI.2004.11.008

[12] Wang Q, Velasco L, Breitung B, Presser V (2021) High-entropy energy materials in the age of big data: a critical guide to next-generation synthesis and applications. Adv Energy Mater 11:2102355. https://doi.org/10.1002/AENM.202102355

[13] Wang K, Huang J, Chen H, Wang Y, Yan W, Yuan X, Song S, Zhang J, Sun X (2022) Recent progress in high entropy alloys for electrocatalysts. Electrochem Energy Rev 5:1–28. https://doi.org/10.1007/S41918-022-00144-8

[14] Cui X, Zhang B, Zeng C, Guo S (2018) Electrocatalytic activity of high-entropy alloys toward oxygen evolution reaction. MRS Commun 8:1230–1235. https://doi.org/10.1557/MRC.2018.111

[15] Wang S, Huo W, Fang F, Xie Z, Shang JK, Jiang J (2022) High entropy alloy/C nanoparticles derived from polymetallic MOF as promising electrocatalysts for alkaline oxygen evolution reaction. Chem Eng J 429:132410. https://doi.org/10.1016/J.CEJ.2021.132410

[16] Ma P, Zhang S, Zhang M, Gu J, Zhang L, Sun Y, Ji W, Fu Z (2020) Hydroxylated high-entropy alloy as highly efficient catalyst for electrochemical oxygen evolution reaction. Sci China Mater 63:2613–2619. https://doi.org/10.1007/S40843-020-1461-2

[17] Zhou P, Wong PK, Niu P, Chen M, Kwok CT, Tang Y, Li R, Wang S, Pan H (2022) Anodized AlCoCrFeNi high-entropy alloy for alkaline water electrolysis with ultra-high performance. Sci China Mater 66:1033–1041. https://doi.org/10.1007/S40843-022-2234-5

[18] Talluri B, Yoo K, Kim J (2022) High entropy spinel metal oxide (CoCrFeMnNi)3O4 nanoparticles as novel efficient electrocatalyst for methanol oxidation and oxygen evolution reactions. J Environ Chem Eng 10:106932. https://doi.org/10.1016/J.JECE.2021.106932

[19] Talluri B, Aparna ML, Sreenivasulu N, Bhattacharya SS, Thomas T (2021) High entropy spinel metal oxide (CoCrFeMnNi)3O4 nanoparticles as a high-performance supercapacitor electrode material. J Energy Storage 42:103004. https://doi.org/10.1016/J.EST.2021.103004

[20] Wang D, Liu Z, Du S, Zhang Y, Li H, Xiao Z, Chen W, Chen R, Wang Y, Zou Y, Wang S (2019) Low-temperature synthesis of small-sized high-entropy oxides for water oxidation. J Mater Chem A Mater 7:24211–24216. https://doi.org/10.1039/C9TA08740K

[21] Wang Z, You J, Zhao Y, Yao R, Liu G, Lu J, Zhao S (2023) Research progress on high entropy alloys and high entropy derivatives as OER catalysts. J Environ Chem Eng 11:109080. https://doi.org/10.1016/J.JECE.2022.109080

[22] Aydinyan S, Kirakosyan H, Sargsyan A, Volobujeva O, Kharatyan S (2022) Solution combustion synthesis of MnFeCoNiCu and (MnFeCoNiCu)3O4 high entropy materials and sintering thereof. Ceram Int 48:20294–20305. https://doi.org/10.1016/J.CERAMINT.2022.03.310

[23] Dąbrowa J, Stygar M, Mikuła A, Knapik A, Mroczka K, Tejchman W, Danielewski M, Martin M (2018) Synthesis and microstructure of the (Co, Cr, Fe, Mn, Ni)3O4 high entropy oxide characterized by spinel structure. Mater Lett 216:32–36. https://doi.org/10.1016/J.MATLET.2017.12.148

[24] Marinko Ž, Suhadolnik L, Samardžija Z, Kovač J, Čeh M (2020) The influence of a surface treatment of metallic titanium on the photocatalytic properties of TiO2 nanotubes grown by anodic oxidation. Catalysts 10:803. https://doi.org/10.3390/CATAL10070803

[25] Lee CY, Lee K, Schmuki P (2013) Anodic formation of self-organized cobalt oxide nanoporous layers. Angew Chem Int Ed 52:2077–2081. https://doi.org/10.1002/ANIE.201208793

[26] Xie K, Guo M, Huang H, Liu Y (2014) Fabrication of iron oxide nanotube arrays by electrochemical anodization. Corros Sci 88:66–75. https://doi.org/10.1016/J.CORSCI.2014.07.019

[27] Shrestha NK, Yang M, Schmuki P (2010) Self-ordered nanoporous nickel oxide/fluoride composite film with strong electrochromic contrast. Electrochem Solid-State Lett 13:C21. https://doi.org/10.1149/1.3430656

[28] Yang Y, Fei H, Ruan G, Xiang C, Tour JM (2022) Efficient electrocatalytic oxygen evolution on amorphous nickelàcobalt binary oxide nanoporous layers. ACS Nano 10:7. https://doi.org/10.1021/nn503760c

[29] Fan J, Chen Z, Shi H, Zhao G (2016) In situ grown, self-supported iron–cobalt–nickel alloy amorphous oxide nanosheets with low overpotential toward water oxidation. Chem Commun 52:4290–4293. https://doi.org/10.1039/C5CC09699E

[30] Kure K, Konno Y, Tsuji E, Skeldon P, Thompson GE, Habazaki H (2012) Formation of self-organized nanoporous anodic films on Type 304 stainless steel. Electrochem commun 21:1–4. https://doi.org/10.1016/J.ELECOM.2012.05.003

[31] Prado LH, Anastasiou E, Virtanen S (2021) Corrosion behavior of anodic self-ordered porous oxide layers on stainless steel. J Electrochem Soc 168:021507. https://doi.org/10.1149/1945-7111/ABE1DE

[32] Schuster JM, Schvezov CE, Rosenberger MR (2023) Polynomial functions for direct calculation of the surface free energy developed from the Neumann equation of state method. Int J Adhes Adhes 124:103370. https://doi.org/10.1016/J.IJADHADH.2023.103370

[33] Kozbial A, Li Z, Conaway C, McGinley R, Dhingra S, Vahdat V, Zhou F, Durso B, Liu H, Li L (2014) Study on the surface energy of graphene by contact angle measurements. Langmuir 30:8598–8606. https://doi.org/10.1021/LA5018328

[34] McCrory CCL, Jung S, Peters JC, Jaramillo TF (2013) Benchmarking heterogeneous electrocatalysts for the oxygen evolution reaction. J Am Chem Soc 135:16977–16987. https://doi.org/10.1021/JA407115P

[35] Zeradjanin AR, Masa J, Spanos I, Schlögl R (2021) Activity and stability of oxides during oxygen evolution reaction–-from mechanistic controversies toward relevant electrocatalytic descriptors. Front Energy Res 8:405. https://doi.org/10.3389/FENRG.2020.613092

[36] Anantharaj S, Noda S (2022) iR drop correction in electrocatalysis: everything one needs to know! J Mater Chem A Mater 10:9348–9354. https://doi.org/10.1039/D2TA01393B

[37] Schalenbach M (2018) Impedance spectroscopy and cyclic voltammetry to determine double layer capacitances and electrochemically active surface areas. https://doi.org/10.1149/OSF.IO/GYEXD

[38] Heidarpour A, Faraji M, Haghighi A (2022) Production and characterization of carbide-derived-nanocarbon structures obtained by HF electrochemical etching of Ti3AlC2. Ceram Int 48:11466–11474. https://doi.org/10.1016/J.CERAMINT.2022.01.003

[39] Besson R (2021) Understanding phase equilibria in high-entropy alloys. II. Atomic-scale study of incorporation of metallic elements in Cr carbides—application to equilibrium with AlCrFeMnMo. J Alloys Compd 874:159959. https://doi.org/10.1016/J.JALLCOM.2021.159959

[40] Chen J, Yao Z, Wang X, Lu Y, Wang X, Liu Y, Fan X (2018) Effect of C content on microstructure and tensile properties of as-cast CoCrFeMnNi high entropy alloy. Mater Chem Phys 210:136–145. https://doi.org/10.1016/J.MATCHEMPHYS.2017.08.011

[41] Tsai KY, Tsai MH, Yeh JW (2013) Sluggish diffusion in Co–Cr–Fe–Mn–Ni high-entropy alloys. Acta Mater 61:4887–4897. https://doi.org/10.1016/J.ACTAMAT.2013.04.058

[42] Pickering EJ, Muñoz-Moreno R, Stone HJ, Jones NG (2016) Precipitation in the equiatomic high-entropy alloy CrMnFeCoNi. Scr Mater 113:106–109. https://doi.org/10.1016/J.SCRIPTAMAT.2015.10.025

[43] Kolawole SK, Kolawole FO, Soboyejo ABO, Soboyejo WO (2019) Modeling studies of corrosion fatigue in a low carbon steel. Cogent Eng 6:1695999. https://doi.org/10.1080/23311916.2019.1695999

[44] Li P, Wan X, Su J, Liu W, Guo Y, Yin H, Wang D (2022) A single-phase FeCoNiMnMo high-entropy alloy oxygen evolution anode working in alkaline solution for over 1000 h. ACS Catal 12:11667–11674. https://doi.org/10.1021/ACSCATAL.2C02946

[45] Wang L, Mercier D, Zanna S, Seyeux A, Laurent-Brocq M, Perrière L, Guillot I, Marcus P (2020) Study of the surface oxides and corrosion behaviour of an equiatomic CoCrFeMnNi high entropy alloy by XPS and ToF-SIMS. Corros Sci 167:108507. https://doi.org/10.1016/J.CORSCI.2020.108507

[46] Li P, Du M (2022) Effect of chloride ion content on pitting corrosion of dispersion-strengthened-high-strength steel. Corros Commun 7:23–34. https://doi.org/10.1016/J.CORCOM.2022.03.005

[47] Farrag HH, Abbas AA, Sayed SY, Alalawy HH, El-Anadouli BE, Mohammad AM, Allam NK (2018) From rusting to solar power plants: a successful nano-pattering of stainless steel 316L for visible light-induced photoelectrocatalytic water splitting. ACS Sustain Chem Eng 6:17352–17358. https://doi.org/10.1021/ACSSUSCHEMENG.8B04899

[48] McKay F, Fang Y, Kizilkaya O, Singh P, Johnson DD, Roy A, Young DP, Sprunger PT, Flake JC, Shelton WA, Xu Y (2021) CoCrFeNi high-entropy alloy as an enhanced hydrogen evolution catalyst in an acidic solution. J Phys Chem C 125:17008–17018. https://doi.org/10.1021/ACS.JPCC.1C03646

[49] Jiang D, Li Z, Xu J, Ren Q, Agbedor SO, Lei Q (2022) High-temperature oxidation behaviors of an equiatomic CrMnFeCoNi high entropy alloy. Mater Today Commun 32:104185. https://doi.org/10.1016/J.MTCOMM.2022.104185

[50] Grzesik Z, Smoła G, Miszczak M, Stygar M, Dąbrowa J, Zajusz M, Świerczek K, Danielewski M (2020) Defect structure and transport properties of (Co, Cr, Fe, Mn, Ni)3O4 spinel-structured high entropy oxide. J Eur Ceram Soc 40:835–839. https://doi.org/10.1016/J.JEURCERAMSOC.2019.10.026

[51] Ungár T (2004) Microstructural parameters from X-ray diffraction peak broadening. Scr Mater 51:777–781. https://doi.org/10.1016/J.SCRIPTAMAT.2004.05.007

[52] Hosterman BD, Raman (2011) Raman Spectroscopic Study of Solid Solution Spinel Oxides. PhD Dissertation, University of Nevada. https://doi.org/10.34917/2476131

[53] Menezes PW, Indra A, González-Flores D, Sahraie NR, Zaharieva I, Schwarze M, Strasser P, Dau H, Driess M (2015) High-performance oxygen redox catalysis with multifunctional cobalt oxide nanochains: morphology-dependent activity. ACS Catal 5:2017–2027. https://doi.org/10.1021/CS501724V

[54] Wang S, Xu B, Huo W, Feng H, Zhou X, Fang F, Xie Z, Shang JK, Jiang J (2022) Efficient FeCoNiCuPd thin-film electrocatalyst for alkaline oxygen and hydrogen evolution reactions. Appl Catal B 313:121472. https://doi.org/10.1016/J.APCATB.2022.121472

[55] You T, Niwa O, Chen Z, Hayashi K, Tomita M, Hirono S (2003) An amperometric detector formed of highly dispersed Ni nanoparticles embedded in a graphite-like

carbon film electrode for sugar determination. Anal Chem 75:5191–5196. https://doi.org/10.1021/AC034204K

[56] Ilton ES, Post JE, Heaney PJ, Ling FT, Kerisit SN (2016) XPS determination of Mn oxidation states in Mn (hydr) oxides. Appl Surf Sci 366:475–485. https://doi.org/10.1016/J.APSUSC.2015.12.159

[57] Einert M, Mellin M, Bahadorani N, Dietz C, Lauterbach S, Hofmann JP (2022) Mesoporous high-entropy oxide thin films: electrocatalytic water oxidation on high-surface-area spinel (Cr0.2Mn0.2Fe0.2Co0.2Ni0.2)3O4 electrodes. ACS Appl Energy Mater 5:717–730. https://doi.org/10.1021/ACSAEM.1C03190

[58] Wang H-Y, Hsu Y-Y, Chen R, Chan T-S, Ming Chen H, Liu B, Wang H, Chen R, Liu B, Hsu Y, Chen HM, Chan T (2015) Ni3+-induced formation of active NiOOH on the spinel Ni–Co oxide surface for efficient oxygen evolution reaction. Adv Energy Mater 5:1500091. https://doi.org/10.1002/AENM.201500091

[59] Raveendran A, Chandran M, Dhanusuraman R (2023) A comprehensive review on the electrochemical parameters and recent material development of electrochemical water splitting electrocatalysts. RSC Adv 13:3843–3876. https://doi.org/10.1039/D2RA07642J

[60] Fabbri E, Habereder A, Waltar K, Kötz R, Schmidt TJ (2014) Developments and perspectives of oxide-based catalysts for the oxygen evolution reaction. Catal Sci Technol 4:3800–3821. https://doi.org/10.1039/C4CY00669K

[61] Lazanas AC, Prodromidis MI (2022) Electrochemical impedance spectroscopy—a tutorial. ACS Meas Sci Au 3:162–193. https://doi.org/10.1021/ACSMEASURESCIAU.2C00070

[62] Wang H, Wei R, Li X, Ma X, Hao X, Guan G (2021) Nanostructured amorphous Fe29Co27Ni23Si9B12 high-entropy-alloy: an efficient electrocatalyst for oxygen evolution reaction. J Mater Sci Technol 68:191–198. https://doi.org/10.1016/J.JMST.2020.06.045

[63] Wang D, Duan C, He H, Wang Z, Zheng R, Sun H, Liu Y, Liu C (2023) Microwave solvothermal synthesis of component-tunable high-entropy oxides as high-efficient and stable electrocatalysts for oxygen evolution reaction. J Colloid Interface Sci 646:89–97. https://doi.org/10.1016/J.JCIS.2023.05.043

[64] Tang J, Xu JL, Ye ZG, Li XB, Luo JM (2021) Microwave sintered porous CoCrFeNiMo high entropy alloy as an efficient electrocatalyst for alkaline oxygen evolution reaction. J Mater Sci Technol 79:171–177. https://doi.org/10.1016/J.JMST.2020.10.079

[65] Connor P, Schuch J, Kaiser B, Jaegermann W (2020) The determination of electrochemical active surface area and specific capacity revisited for the system MnOx as an oxygen evolution catalyst. Z fur Phys Chem 234:979–994. https://doi.org/10.1515/ZPCH-2019-1514

[66] Zistler M, Wachter P, Schreiner C, Ott S, Du F, Lopez Luna M, Morales DM, Risch M (2021) Seven steps to reliable cyclic voltammetry measurements for the determination of double layer capacitance. J Phys Energy 3:034013. https://doi.org/10.1088/2515-7655/ABEE33

[67] Park H, Bae JW, Lee TH, Park IJ, Kim C, Lee MG, Lee SA, Yang JW, Choi MJ, Hong SH, Kim SY, Ahn SH, Kim JY, Kim HS, Jang HW (2022) Surface-tailored medium entropy alloys as radically low overpotential oxygen evolution electrocatalysts. Small 18:2105611. https://doi.org/10.1002/SMLL.202105611

[68] Tahir M, Pan L, Idrees F, Zhang X, Wang L, Zou JJ, Wang ZL (2017) Electrocatalytic oxygen evolution reaction for energy conversion and storage: a comprehensive review. Nano Energy 37:136–157. https://doi.org/10.1016/J.NANOEN.2017.05.022

[69] Kwok DY, Neumann AW (1999) Contact angle measurement and contact angle interpretation. Adv Colloid Interface Sci 81:167–249. https://doi.org/10.1016/S0001-8686(98)00087-6

[70] Burrow J (2018) Surface area and electrocatalytic properties of FeNi surface area and electrocatalytic properties of FeNi Nanoparticles for the Oxygen Evolution Reaction (OER). Undergraduate Theses, University of Arkansas

[71] Huang K, Peng D, Yao Z, Xia J, Zhang B, Liu H, Chen Z, Wu F, Wu J, Huang Y (2021) Cathodic plasma driven self-assembly of HEAs dendrites by pure single FCC FeCoNiMnCu nanoparticles as high efficient electrocatalysts for OER. Chem Eng J 425:131533. https://doi.org/10.1016/J.CEJ.2021.131533

[72] Albedwawi SH, AlJaberi A, Haidemenopoulos GN, Polychronopoulou K (2021) High entropy oxides-exploring a paradigm of promising catalysts: A review. Mater Des 202:109534. https://doi.org/10.1016/J.MATDES.2021.109534

[73] Gao Y, Liu Y, Yu H, Zou D (2022) High-entropy oxides for catalysis: Status and perspectives. Appl Catal A Gen 631:118478. https://doi.org/10.1016/J.APCATA.2022.118478

[74] Feng M, Huang J, Peng Y, Huang C, Yue X, Huang S (2022) Tuning electronic structures of transition metal carbides to boost oxygen evolution reactions in acidic medium. ACS Nano 16:13834–13844. https://doi.org/10.1021/ACSNANO.2C02099

[75] Abdelhafiz A, Wang B, Harutyunyan AR, Li J (2022) Carbothermal shock synthesis of high entropy oxide catalysts: dynamic structural and chemical reconstruction boosting the catalytic activity and stability toward oxygen evolution

reaction. Adv Energy Mater 12:2200742. https://doi.org/10.1002/AENM.202200742

[76] Pan Y, Xu X, Zhong Y, Ge L, Chen Y, Veder JPM, Guan D, O'Hayre R, Li M, Wang G, Wang H, Zhou W, Shao Z (2020) Direct evidence of boosted oxygen evolution over perovskite by enhanced lattice oxygen participation. Nat Commun 11:2002. https://doi.org/10.1038/S41467-020-15873-X

[77] Chen FY, Wu ZY, Adler Z, Wang H (2021) Stability challenges of electrocatalytic oxygen evolution reaction: from mechanistic understanding to reactor design. Joule 5:1704–1731. https://doi.org/10.1016/J.JOULE.2021.05.005